

Tailoring the Electrocatalytic Activity and Corrosion Resistance of CoCrFeNi and MnCrFeNi Thin Films by Anodization

Clara Linder,* Mikhail Vagin, Robert Boyd, Grzegorz Greczynski, Daniel Lundin, Karin Törne, Per Eklund, and Emma M. Björk

Transition metal oxides like Co, Ni, and Mn are promising alternatives to noble metals such as Pt for oxygen electrocatalysis in green energy. Alloying these metals forms multicomponent catalysts with compelling properties. In this study, CoCrFeNi and MnCrFeNi thin films are synthesized using High-Power Impulse Magnetron Sputtering (HiPIMS) and their catalytic activity for the Oxygen Reduction Reaction (ORR), the Oxygen Evolution Reaction (OER), and corrosion resistance in 1 molar (1 M) potassium hydroxide (KOH) are evaluated. MnCrFeNi films exhibit a fine-grained single face-centered cubic (FCC) phase, while CoCrFeNi films have larger grains and multiple phases. ORR on CoCrFeNi follows a 2+1 electron transfer pathway, producing hydroxide radicals, while MnCrFeNi exhibits a 2-electron pathway, yielding hydrogen peroxide. Anodization reduces the CoCrFeNi overpotential from 0.9 to 0.5 V versus the reversible hydrogen electrode (RHE), comparable to platinum and iridium catalysts (Pt/C, Ir/C). Anodization also shifts CoCrFeNi ORR to a 2-electron pathway. In situ Raman spectroscopy detects no ORR intermediates, but nickel oxyhydroxide (NiOOH) appears during OER. Substituting Mn for Co increases corrosion resistance by raising the corrosion potential. All films show passive behavior during polarization, demonstrating their potential for corrosion protection and electrocatalysis in green energy applications.

1. Introduction

Oxygen Reduction Reaction (ORR) together with Hydrogen Oxidation Reaction (HOR) are the key electrochemical reactions in devices based on water recombination that can generate fossil-free electricity. The fuel used in the devices are oxygen and hydrogen gases which can be produced by the reverse reactions Oxygen Evolution Reaction (OER) and Hydrogen Evolution Reaction (HER), that is, water splitting. ORR and OER have slow and sluggish kinetics, and catalysts are needed for efficient application in devices such as Anion Exchange Membrane Fuel Cells and Electrolyzers.^[1-3] Today, these devices are based on noble metal catalysts, for example, Pt, Pd, and Ru, because of their high activity and chemical stability. However, the high cost and scarcity of these elements limit scaling up of these important technologies, which motivates the search for other cheaper and

C. Linder, K. Törne
RISE
Corrosion
Vehicles and Surface Protection
Kista 164 40, Sweden
E-mail: clara.linder@ri.se

C. Linder, R. Boyd, E. M. Björk
Nanostructured Materials
Department of Physics
Chemistry and Biology (IFM)
Linköping University
Linköping 581 83, Sweden

 The ORCID identification number(s) for the author(s) of this article can be found under <https://doi.org/10.1002/adsu.202400797>

© 2025 The Author(s). Advanced Sustainable Systems published by Wiley-VCH GmbH. This is an open access article under the terms of the [Creative Commons Attribution](https://creativecommons.org/licenses/by/4.0/) License, which permits use, distribution and reproduction in any medium, provided the original work is properly cited.

DOI: [10.1002/adsu.202400797](https://doi.org/10.1002/adsu.202400797)

M. Vagin
Laboratory of Organic Electronics
Department of Science and Technology
Linköping University
Norrköping 601 74, Sweden

G. Greczynski, P. Eklund
Thin Film Physics Division
Department of Physics
Chemistry
and Biology (IFM)
Linköping University
Linköping 581 83, Sweden

D. Lundin
Plasma and Coatings Physics Division
Department of Physics
Chemistry
and Biology (IFM)
Linköping University
Linköping 581 83, Sweden

more abundant alternatives. Potential candidates are 3d transition metals and their oxides, such as Co_3O_4 ,^[4] NiO ,^[5] Fe_2O_3 ,^[6] Mn_3O_4 ,^[7] Mn_2O_3 and MnO_2 ,^[8] or a combination of spinel oxides NiCo_2O_4 ,^[9] CoMn_2O_4 ,^[10] and $\text{Mn}_x\text{Fe}_{3-x}\text{O}_4$.^[11] These have all shown promising catalytic performance, comparable to those of noble metal catalysts.

The 3d metals can also be alloyed together to form multicomponent catalysts. When at least four elements are present, and the composition of each element is near equimolar, the alloys belong to the High Entropy Alloy (HEA) family. The Cantor alloy CoCrFeNiMn was one of the first HEA to be discovered in 2004^[12] and has since then been investigated as multicomponent catalysts.^[13] Löffler et al.^[14] used sputtering into ionic liquids to synthesize CoCrFeNiMn based nanoparticles and tested them for ORR. They found that Mn played an important role in increasing the performance of the multi-material catalysts. High Co and Fe content in CoCrFeNiMo films was found to be beneficial for HER activity.^[15] In our previous study,^[16] magnetron sputtering was used to deposit thin films of CoCrFeNi with various Fe content. The films were active toward ORR, and it was observed that Fe had a synergistic effect with the other active sites that impacted the catalytic activity of the films.

To further improve the catalytic activity of the multicomponent system, additional active sites can be generated by modifying the surface of the catalyst. Anodization can be used to electrochemically alter the oxidation state of the surface and has been shown to improve the ORR performance of pure Co and CoCrFeNi thin films by increasing the amount of active sites^[4,16,17] and has yet to be investigated for Mn based films.

While both Mn and Co are active for oxygen reaction catalysis, there is an interest to find abundant, conflict-free, cheap, and non-toxic alternatives to noble metals. In this sense, Mn has several advantages over Co.^[18] Furthermore, Mn has three oxide forms, MnO_2 , Mn_2O_3 , and Mn_3O_4 that have been reported as active catalysts,^[19] whereas Co has mainly two, $\text{Co}(\text{OH})_2$ and Co_3O_4 .

To optimize the catalyst performance, there is a need for in depth understanding of the correlation between the catalyst structure, composition, and the underlying catalytic mechanism. The electrochemical pathway for the oxygen reaction is determined by the number of electrons transferred. For OER, it is a 4-electron transfer pathway. Whereas for ORR, either the 4-electron transfer reaction which produces hydroxide ions as a product or the 2-electron transfer that produces hydrogen peroxide. The pathway taken affects the amount of energy produced and the devices efficiency. Although 2-electron ORR produces less electric energy, it has the advantage of producing valuable oxidants such as hydrogen peroxide or hydroxyl radicals for pollutant degradation and water treatments.^[20]

In addition to the electrochemical pathway taken by the catalysts, their chemical stability is also of interest, for example, investigating if there is an irreversible interaction of the catalyst with the oxygen molecules. The stability of $\text{NiMoO}_4@\text{Co}_3\text{O}_4$ nanorods,^[21] CoCrFeNi films^[22] and Ni–Fe layered double hy-

droxides layers^[23] have been investigated by Raman spectroscopy, where the formation of NiOOH and significant changes in the Ni–O bonds were observed during OER.

This study investigates the electrocatalytic mechanisms of CoCrFeNi and MnCrFeNi films for both OER and ORR in KOH. We demonstrate that anodization can be used to electrochemically tailor surface oxidation through surface analysis and electrocatalytic performance tests. An enhancement toward both ORR and OER was observed after anodization for both films. In addition, the corrosion resistance of the films is investigated to evaluate their suitability in alkaline fuel cells and electrolyzers. This study aims to provide information on how to better select and design 3d transition metal electrocatalysts as thin films for green energy applications.

2. Results

2.1. Thin Films Structure

The composition of the CoCrFeNi and MnCrFeNi films deposited on steel substrates was determined using energy dispersive spectroscopy (EDS) and the results are shown in **Table 1**.

Figure 1a,c show top view scanning electron microscopy (SEM) images of CoCrFeNi and MnCrFeNi films. Both films appear to have a grain structure, with significantly larger grains for the CoCrFeNi films (approx. 60 nm) compared to the MnCrFeNi films (20 nm). For the CoCrFeNi films, the cross sectional high angle annular dark field scanning transmission electron microscopy (HAADF-STEM) images (**Figure 1b** shows the characteristic columnar grain structure typically seen for physical vapor deposition and high-power impulse magnetron sputtering (HiPIMS) deposited films, although with a high concentration of defects, probably stacking faults. **Figure 1d** shows the corresponding image for the MnCrFeNi films which also shows a columnar structure, which are significantly thinner compared to the CoCrFeNi films. Underdense grain boundaries leading to pores are evident in the top part of the films (after 100 nm of film thickness) along with an apparent nanostructure indicating a possible sub-grains and heterogeneities within the columns themselves.

The film thickness is significantly smaller for the MnCrFeNi films compared to CoCrFeNi films (210 nm vs 350 nm in thickness).

Figure 2 shows X-ray diffractograms of the steel substrate, CoCrFeNi , and MnCrFeNi films.

For the CoCrFeNi film three different phases have been identified: an face-centered cubic (FCC) with a 111 preferred orientation with a peak at 44° and two secondary phases, an hexagonal close packed (HCP), and a tetragonal sigma with lower peak intensity at 47° and $40\text{--}42^\circ$ respectively. For MnCrFeNi only one phase was identified, the FCC phase same as for CoCrFeNi but much broader due to the small grain size.

2.2. Electrochemical Modification of the Films by Anodization

Anodization was used to modify the surface oxidation states of the films. The surfaces of the films were analyzed by X-ray

P. Eklund
Department of Chemistry – Ångström
Uppsala University
Uppsala 751 21, Sweden

Table 1. Atomic percentage of the films determined by EDS.

at. %	Co	Cr	Mn	Fe	Ni
CoCrFeNi	30.1 ± 0.3	22.5 ± 0.4	–	22.3 ± 0.3	25.1 ± 0.2
MnCrFeNi	–	28.1 ± 0.4	23.7 ± 0.4	24.0 ± 0.2	24.3 ± 0.2

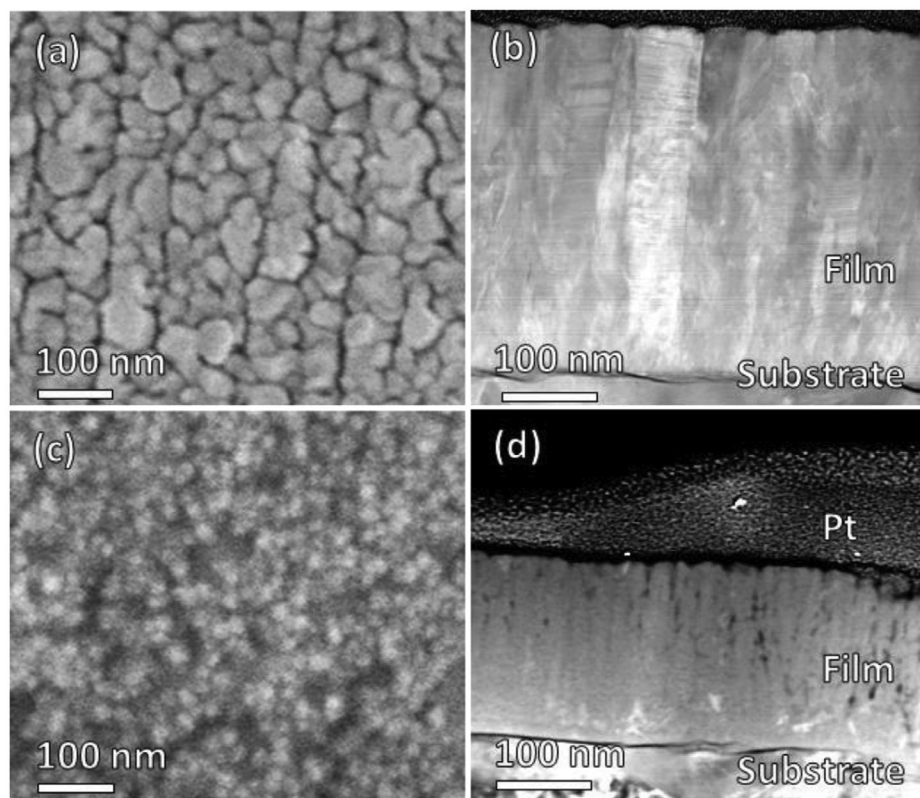


Figure 1. SEM top view images (a) CoCrFeNi films, (c) MnCrFeNi films and STEM cross-section micrographs (b) CoCrFeNi films, (d) MnCrFeNi films.

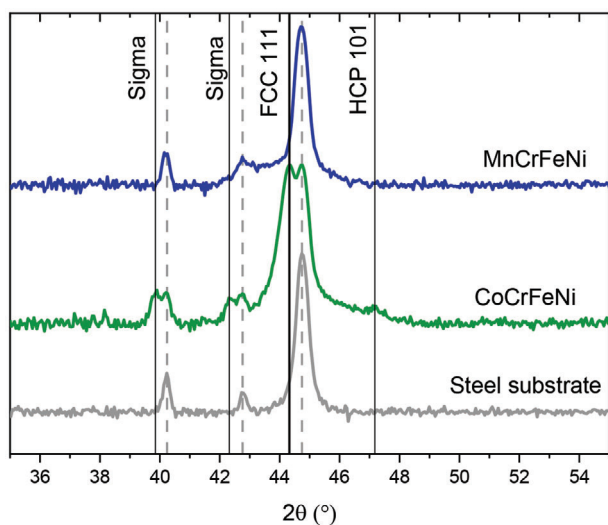


Figure 2. X-ray diffractograms of CoCrFeNi, MnCrFeNi films grown on steel plates. The film peaks are marked by full lines, and dashed lines correspond to substrate peaks.

photoelectron spectroscopy (XPS). As a reference, as-deposited films were immersed for 30 min in KOH without any electrochemical measurements. The results are shown in **Figure 3**. All films have oxidized metal species, both oxides and hydroxides, on their surface. For films exposed to KOH, metal–metal bonds are also present in distinct relative intensity compared to the anodized films. Anodization enriches the surface either in Co or Mn cations and in Ni for both films, while there is a lower Fe and Cr content in comparison to the films only exposed to KOH. To estimate the thickness of the top oxide layers, XPS sputter depth profiles were acquired, revealing the metallic bonds in the anodized films (see **Figure S1**, Supporting Information). For MnCrFeNi anodized films, metallic bonds for Ni, Mn and Fe become clearly visible after removing the top 2.8 nm, indicating that a fully oxidized surface layer is formed upon anodization. For the other films, the oxidized layer is thinner, and the metallic components in core level spectra appear already at 1.4 nm below the surface. Underneath the oxidized layer, the oxygen content is still significant, indicating a mix of metals and metal oxides and that oxygen diffuses deeper into the film.

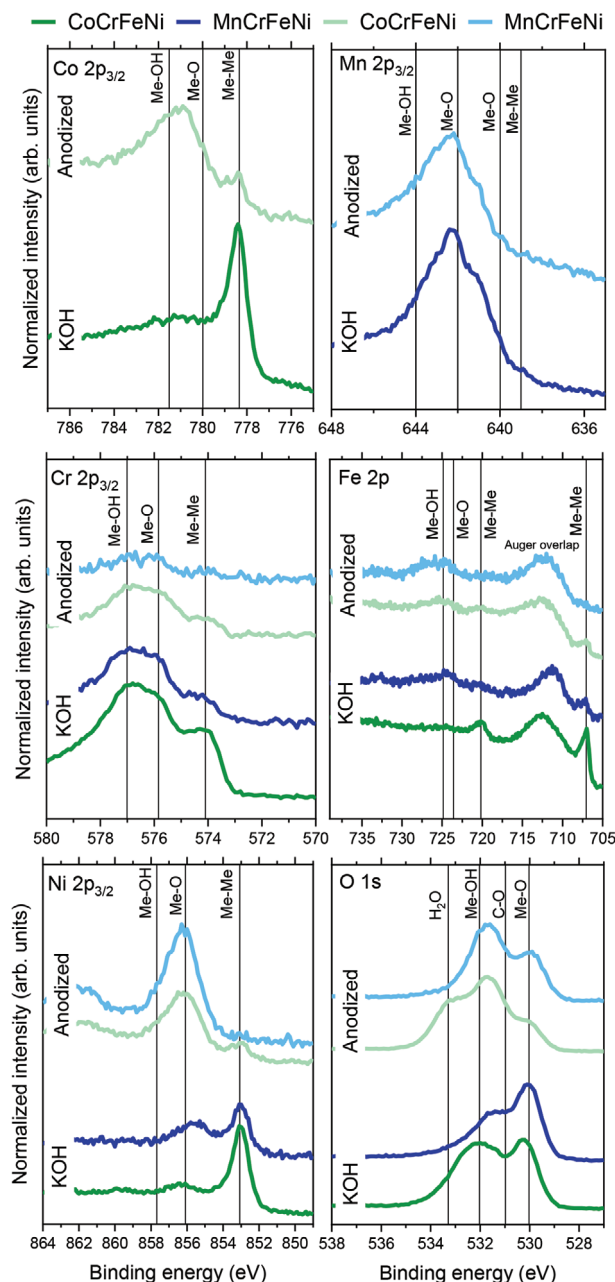


Figure 3. XPS core level spectra of CoCrFeNi and MnCrFeNi films exposed to KOH and after anodization.

2.3. ORR and OER Evaluation

Figure 4 shows the ORR and OER performance of the films. **Table 2** presents the extracted values for the ORR onset potential, whereas for OER the potential was extracted at 10 mA cm^{-2} .

All films were active toward both ORR and OER in both as-deposited and anodized state. MnCrFeNi films had lower ORR and OER onset potentials than CoCrFeNi films. Anodization further decreased both the OER potential and the ORR potential for CoCrFeNi (**Table 2**).

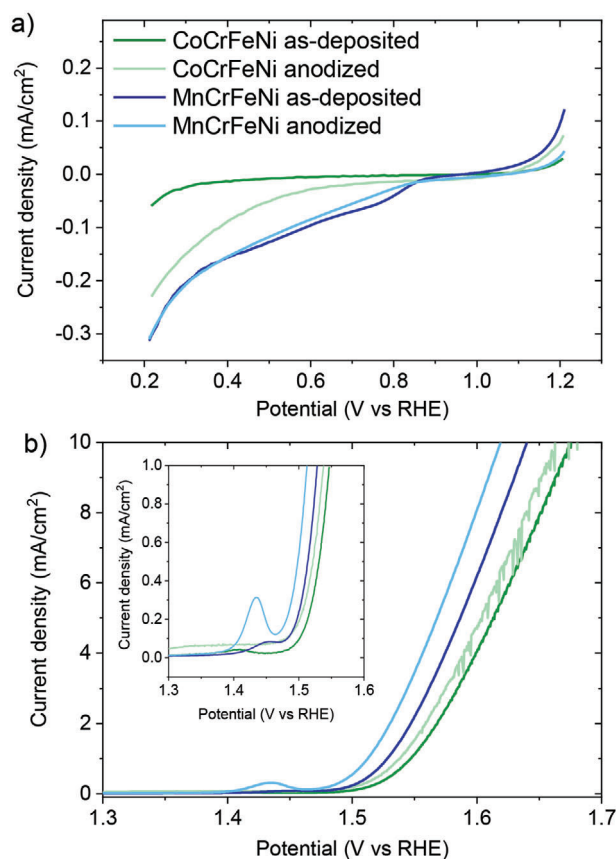


Figure 4. Linear sweep voltammetry for ORR (a) and OER (b) of as-deposited and anodized CoCrFeNi and MnCrFeNi films.

A peak $\approx 1.4\text{--}1.45 \text{ V}$, prior to the start of OER, was observed for all films and was attributed to the $\text{Ni}^{2+}/\text{Ni}^{3+}$ redox couple. After anodization, the $\text{Ni}^{2+}/\text{Ni}^{3+}$ peak becomes more evident for MnCrFeNi. The Tafel slopes of the MnCrFeNi are lower than the CoCrFeNi films for both ORR and OER (**Table 2**), which indicates that the rate limiting step and the kinetics of the reactions are different.

2.4. Film Evolution During ORR and OER

CoCrFeNi and MnCrFeNi films were deposited on Ni foam as a flexible substrate adapted for in situ Raman studies. The same film structure as on the steel substrates is observed on the foam (**Figure S2**, Supporting Information). The foams were electrochemically polarized at 0.2 V versus RHE for ORR and 1.5 V for OER, based on **Figure 4** and the Raman spectra are shown in **Figure 5**.

For ORR (0.2 V) there are no significant peaks detected, indicating that there is no apparent change in the chemical structure of the films. For OER (1.5 V), two distinctive peaks are seen at 468 and 551 cm^{-1} . These peaks are attributed to NiOOH, seen at 480 and 560 cm^{-1} for Ni-based catalysts.^[21,24] Lee et al. reported a shift of the NiOOH peaks toward lower frequencies was observed for catalysts containing Fe in addition to Ni.^[23] For the MnCrFeNi as deposited film, an additional peak is seen

Table 2. ORR and OER parameters extracted from Figure 3.

		ORR		OER	
		Onset potential (V vs RHE)	Tafel slope (mV/dec)	Potential at 10 mA cm ⁻² (V vs RHE)	Tafel slope (mV/dec)
CoCrFeNi	As-deposited	0.34	476	1.66	52
	Anodized	0.76	366	1.66	51
MnCrFeNi	As-deposited	0.88	104	1.64	46
	Anodized	0.89	128	1.62	42

≈780 cm⁻¹ and is attributed to NiOO⁻ bonds.^[25] This peak is also observed for the Ni foam substrate. No distinctive contribution of Co could be detected for the CoCrFeNi films.

2.5. ORR Mechanism

To determine the ORR pathway for the CoCrFeNi and MnCrFeNi films, a Koutecky-Levich study was conducted with a rotating ring disk electrode (RRDE) (Figure S3, Supporting Information) to determine the number of transferred electrons *n* and the Tafel slopes based on the kinetic current (Figure 6a–c). Additional information about the in situ intermediate product H₂O₂ yield was obtained by analyzing the ring current of the RRDE (Figure 6d,e). The number of transferred electrons increases with potential, reaching a maximum value of 2.6 and 2.1 electrons for as-deposited CoCrFeNi and MnCrFeNi, respectively. The number reported for Pt/C and recent Fe₃C@CNT is 4 electrons.^[26]

Anodization decreased the calculated number of transferred electrons for both films. For CoCrFeNi, the Tafel slopes slightly decreased (from 185 to 167 mV dec⁻¹) after anodization and are approaching the theoretical value of 120 mV dec⁻¹. For MnCrFeNi the slope values are much higher than the theoretical values and increase after anodization. The Tafel values from the RRDE differ from the Tafel slopes retrieved with the stationary electrode, Figure 3 and Table 2. The Tafel extrapolation in Figure 3 was performed close to the onset potential of ORR, 0.4–0.8 V where the current starts to increase. This increase of current in this potential region was not observed in the RRDE measurements, indicating a mass transport dependence.

2.6. Corrosion Resistance

The electrochemical impedance spectroscopy (EIS) and potentiodynamic polarization measurements recorded in 1 M KOH are shown in Figure 7.

Bode plots show that CoCrFeNi has a higher total impedance and charge transfer resistance than the MnCrFeNi films, indicating that the overall corrosion resistance of the Co based films is higher. After anodization, the impedance and resistance decrease for CoCrFeNi, whereas for MnCrFeNi they remain the same. The maximum phase angle of the films is also decreases after anodization and shift toward lower frequencies. To further quantify the resistance, the data was fitted with an equivalent electronic circuit based on prior knowledge of the passive film structure in alkaline environments.^[16,27] The circuit consists of different components: resistors and constant phase elements (CPE). The CPE

is used to model a non-ideal capacitor and considers the heterogeneity at the thin film surface. Its impedance can be written as $Z_{CPE} = 1/[Y_0(j\omega)^n]$, where Z_{CPE} is the impedance for the CPE, Y_0 the modulus, j the complex number, ω the angular frequency and n the correction factor ($n = 1$ when the capacitor is ideal and $0.5 < n < 1$ when it is non-ideal). R_s and R_{ct} are resistors which models the resistance of the solution and the charge transfer resistance respectively. The extracted parameters are shown in Table 3. For CoCrFeNi the charge transfer resistance decreased significantly after anodization, whereas for MnCrFeNi no difference was observed.

In the polarization curves, all films have a passive region after the corrosion potential. That region extends until 0.5 V where the transpassive and OER region starts. A Tafel extrapolation was carried out to extract the corrosion potential E_{corr} , corrosion current density i_{corr} , and the passive current density i_{pass} and is shown in Table 3. The corrosion potential of the CoCrFeNi films is lower than the MnCrFeNi, indicating an ennoblement and increase of the corrosion resistance of the films when replacing Co with Mn. The corrosion current densities, which are proportional the corrosion rates, are higher for MnCrFeNi than CoCrFeNi, but the passive current densities are in the same range. This indicates that the CoCrFeNi are likely to corrode less in the early stages of corrosion but once the passive film has stabilized the films have the same behavior. Anodization reduced the corrosion resistance of CoCrFeNi as the total impedance detected by EIS decreased, but nonetheless, the passive behavior in the polarization curves and high R_{ct} values indicate a high corrosion resistance of CoCrFeNi.

3. Discussion

3.1. Thin Film Structure

The different crystal structures for CoCrFeNi and MnCrFeNi thin films (Figures 1 and 2) are attributed to the film compositions. Mn is a well-known FCC stabilizer for the Cantor alloy as a bulk material,^[28] which is likely the case for films as well. Lattice distortions, the presence of defects, and the tendency of Co to form HCP phases are probable reasons for the presence of multiple phases in CoCrFeNi films.^[16,29]

MnCrFeNi has a smaller grain size, in terms of column width and sub-grains within the columns themselves compared to CoCrFeNi, seen in the SEM micrographs and X-ray diffractograms. This is attributed to repeated nucleation, that is, hindered growth followed by new nucleation sites throughout the film growth,^[30] similarly to what has been observed for Cu–Mn

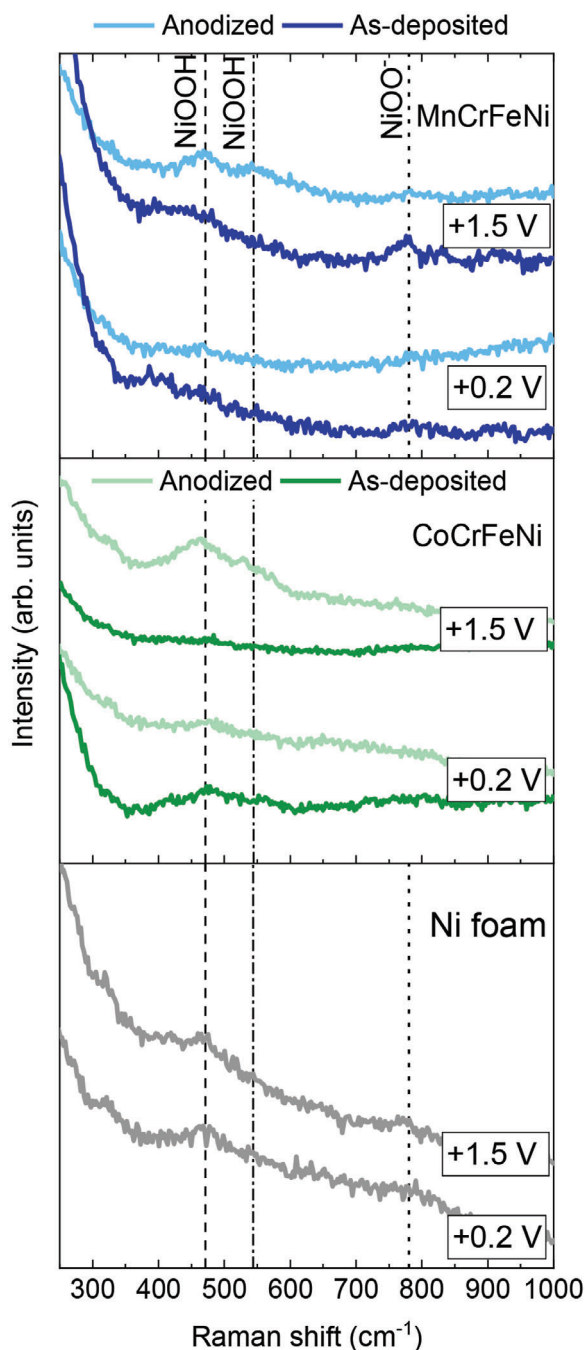


Figure 5. Raman spectra of Ni foam substrate, CoCrFeNi, and MnCrFeNi films (as-deposited and anodized), polarized at OER and ORR potentials.

sputtered films.^[31] The altered growth of the MnCrFeNi films after 100 nm in thickness is also believed to be the cause of increased porosity in the films.

3.2. ORR and OER Catalysis

Both CoCrFeNi and MnCrFeNi films are active for both ORR and OER, they can therefore be classified as bifunctional oxygen reaction catalysts. MnCrFeNi as-deposited has a lower onset poten-

tial than both CoCrFeNi as-deposited and anodized. Adding Mn to a porous Fe oxide and in CoCrFeNi nanoparticles has previously been shown to considerably improve the ORR and OER activity.^[11,14] Mn increases the valency of Co in Mn-Co₃O₄ which promotes electron transfer,^[32] thus the higher performance of the MnCrFeNi film is attributed to Mn and its effect on the other active elements Fe and Ni.

The activity of the films is attributed to the presence of active sites, namely Co²⁺, Co³⁺ or Mn²⁺, Mn³⁺, and Ni²⁺, Ni³⁺. Anodization increases the amount of active sites at the surface of the film which improves the catalytic activity, for example, reduces the overpotential to initiate the reaction (Figures 4 and 6). While anodization did have a significant effect on CoCrFeNi for ORR, the difference was not as pronounced for MnCrFeNi. MnCrFeNi exposed to KOH had oxidized species, in particular Mn cations (Figure 3), whereas CoCrFeNi has mostly metallic bonds when only exposed to KOH. Thus, the effect on the oxidation state is most clearly seen for CoCrFeNi.

In the cyclic voltametry for OER testing, a peak prior to the onset of OER was recorded, which is attributed to NiOOH and the Ni²⁺/Ni³⁺ redox couple in agreement with previous studies.^[23,33] NiOOH was also identified by in situ Raman studies for the anodized films, where the two peaks for Ni–O bonds were recorded. The shift of the peaks is attributed to the presence of Fe that stretches the Ni–O bonds and results in higher structural disorder on the surface of the films.^[23] For ORR, no significant peak was detected for the films, indicating either that there is no noteworthy change in the surface chemistry of the films or that the changes are too small to be detected.

3.3. ORR Pathway

To determine the ORR pathways taken by the CoCrFeNi and MnCrFeNi films and evaluate how much hydrogen peroxide was produced, in situ, RRDE measurements were performed. The maximum number of transferred electrons *n* for CoCrFeNi was 2.6 for as deposited and 2.1 after anodization. The H₂O₂ yield for the as-deposited CoCrFeNi films was low (< 20%) which supports a 2+1 electron transfer where the H₂O₂ reacts with Fe, Co, or Ni cations in a Fenton reaction to form hydroxide radicals.^[9,34,35] After anodization the H₂O₂ yield is higher (30–40%) than the as-deposited films, which indicates a 2-electron ORR mechanism and no formation of radicals. The H₂O₂ yield for the anodized CoCrFeNi is unreasonably high (>1) for potentials > 0 V versus RHE. This is attributed to a low disc current, which makes the ring/disc current ratio high, due to low catalytic activity. The number of transferred electrons is also low (<1). As the number of electrons increases, the H₂O₂ yield decreases as well. For MnCrFeNi, both anodized and as-deposited films, the number of electrons calculated was ≈2.0, indicating the 2-electron pathway for ORR with formation of H₂O₂. The H₂O₂ yield of anodized MnCrFeNi was the highest of all tested films and more constant with potential than the as-deposited film. Mn has been reported to enhance the reactivity of Fe toward H₂O₂ production.^[36] Cr₂O₃ and NiO are also selective toward H₂O₂ production,^[5,9] which are some of the oxides present after anodization (Figure 3).

For the ORR Tafel extrapolation, only one slope was considered resulting in a on step Tafel slope for our catalysts. A first

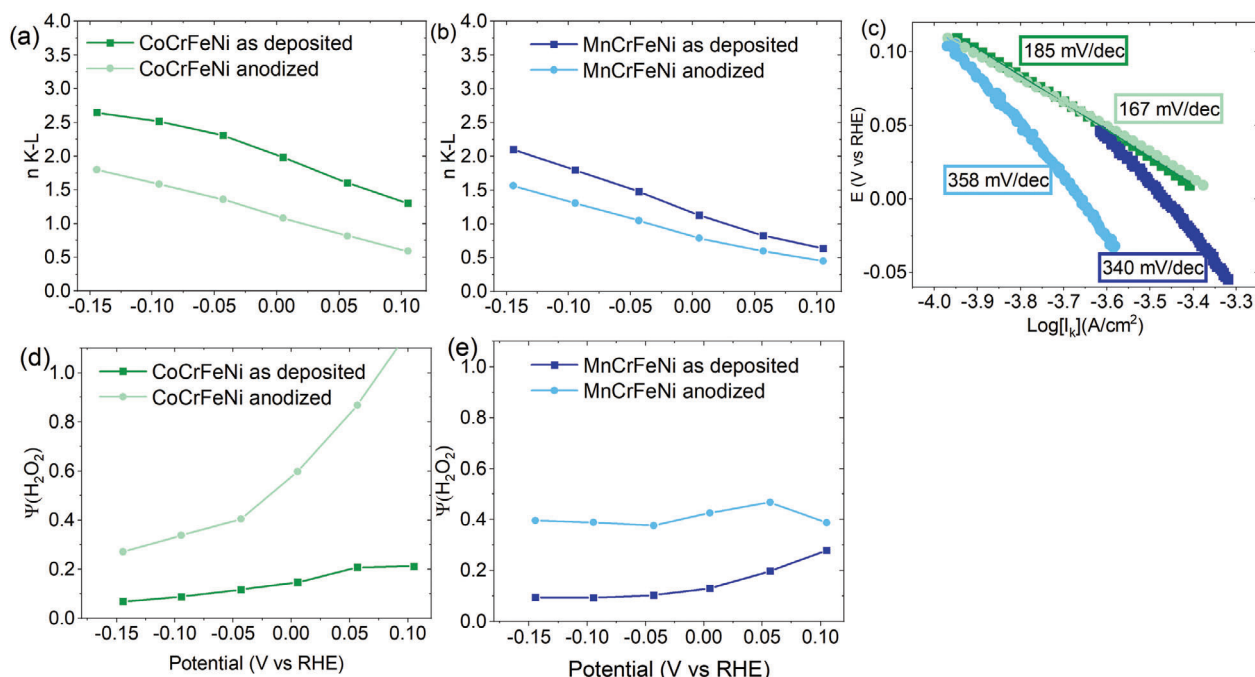


Figure 6. Data extracted from the ORR RRDE study: number of transferred electrons (a-b) Tafel slopes (c) and H_2O_2 yield (d-e).

Table 3. EIS and polarization curve parameters extracted from Figure 7.

		R_{ct} [Ωcm^2]	E_{corr} [V vs Ag/AgCl]	i_{corr} [$\mu\text{A}/\text{cm}^2$]	i_{pass} [$\mu\text{A}/\text{cm}^2$]
CoCrFeNi	As-deposited	$8.7 \times 10^4 \pm 1.9 \times 10^3$	-0.23 ± 0.02	0.09 ± 0.01	16.3 ± 2.5
	Anodized	$1.1 \times 10^4 \pm 2.2 \times 10^3$	-0.15 ± 0.02	0.10 ± 0.05	7.45 ± 6.8
MnCrFeNi	As-deposited	$6.3 \times 10^3 \pm 3.5 \times 10^3$	-0.13 ± 0.01	2.5 ± 1.4	14.2 ± 1.5
	Anodized	$3.1 \times 10^3 \pm 3.9 \times 10^2$	-0.12 ± 0.02	2.3 ± 0.9	27.7 ± 5.8

extrapolation was done for a stationary electrode and a second with the kinetic current extracted from the RRDE measurements. For CoCrFeNi the current density increased only at high overpotentials (≈ 0.3 V vs RHE), whereas MnCrFeNi in the stationary measurements has a change of slope in the current density at 0.8 V versus RHE. This increase of current at low overpotentials was not found in the RRDE measurements. MnCrFeNi are thus likely to be more sensitive to mass transport such as oxygen diffusion. For stationary MnCrFeNi and kinetic currents of CoCrFeNi, the slopes are approaching the 120 mV dec^{-1} theoretical values for the first electron transfer step (electron to the adsorbed oxygen molecule) as the rate determining step.^[37]

3.4. Corrosion Resistance

The corrosion resistance of CoCrFeNi and MnCrFeNi as deposited and anodized films was evaluated in KOH environments. It was observed that MnCrFeNi films had a higher

corrosion potential, that is, an ennoblement of the surface when Mn is replacing Co. MnCrFeNi films have a single FCC phase whereas CoCrFeNi has several (FCC + HCP + sigma) which can be detrimental for the corrosion resistance of multicomponent alloys due to galvanic effects between the phases.^[38,39] Furthermore, the MnCrFeNi films have a much smaller grain size than CoCrFeNi which is also a promoting factor of higher corrosion resistance.^[40] However, the corrosion and passive current densities of the MnCrFeNi films are slightly higher than for the CoCrFeNi films, showing that the corrosion resistance of MnCrFeNi is lower. Similar effects have been observed for Mn additions to CoCrFeNi which was attributed to the suppression of passivity due to Mn dissolutions, increased number of defects, and lack of Cr in the passive films.^[41,42] The MnCrFeNi films are more porous than the columnar CoCrFeNi films, as seen in the cross-section images, which would enable the electrolyte to penetrate the film and lower the corrosion resistance, that is, increase of the corrosion and passive current densities. Nonetheless, all thin films present a passive behavior indicating the corrosion

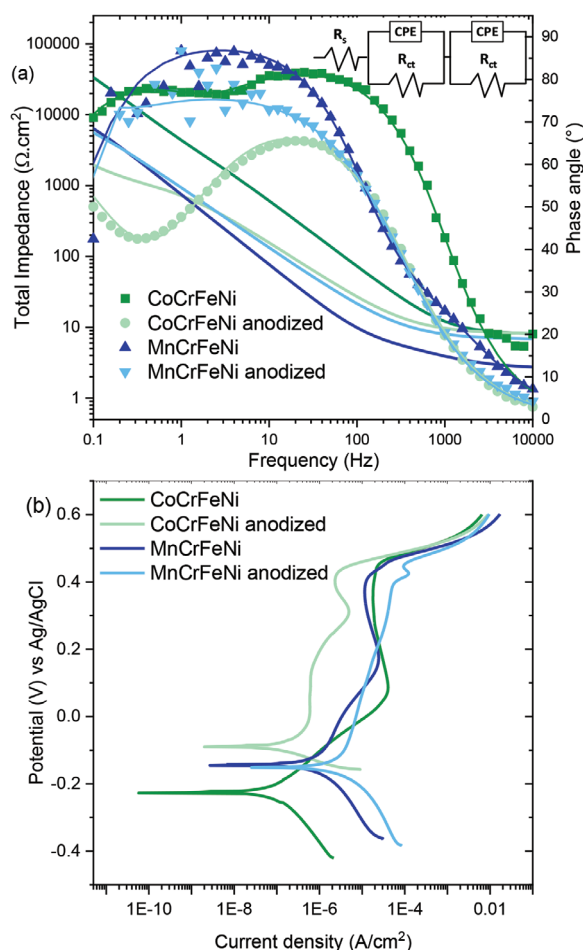


Figure 7. (a) Bode plots from EIS data recorded at OCP for the films, raw data points as symbols and fitted data as lines, and (b) potentiodynamic polarization curves.

process was slowed down once a stable protective passive film had formed. A significant improvement in passive current density after anodization was observed for CoCrFeNi. This is attributed to the formation of a thicker protective oxide layer. The better corrosion performance could also be a result of enrichment of the passive layer in Co which provided better protection.^[43]

4. Conclusion

The present work shows that CoCrFeNi and MnCrFeNi thin films are both active catalysts toward both ORR and OER and have a high corrosion resistance in KOH. For a stationary electrode, MnCrFeNi films have a lower overpotential (0.3 V vs RHE) compared to CoCrFeNi films for ORR, but similar to the overpotential reported for noble metal catalyst.^[1,2] The improvement was not observed with a rotating electrode indicating a diffusion-controlled behavior. For the ORR mechanism, CoCrFeNi tends to give 2+1 electron transfer whereas MnCrFeNi follow the 2-electrons pathway. Electrochemically modifying the surface by anodization decreased the overpotential of CoCrFeNi films and changed the selectivity of the films toward a 2-electron pathway. For ORR, no reaction intermediates were detected by in situ Raman spec-

troscopy. NiOOH was found as an intermediate to OER, identified by spectroscopy and in the cyclic voltammograms. Replacing Co with Mn did increase the corrosion potential, that is, ennoblement of the films and thus improves the corrosion resistance of the film, however, the current densities of MnCrFeNi films were slightly higher than those of CoCrFeNi films. All films showed a passive behavior in the polarization curves, which shows their high corrosion resistance. In summary, the synthesized films are well suited for corrosion protection as well as for oxygen electrocatalysis in alkaline media.

5. Experimental Section

Thin Films Synthesis-HiPIMS Discharge: CoCrFeNi and MnCrFeNi films were deposited on polished carbon steel, polished stainless steel substrates, and Ni foam using HiPIMS discharges.^[44] For CoCrFeNi, three 3-inch (in diameter) targets were used: a CrNi compound target (3 mm thick), an elemental Co target (3 mm thick), and an elemental Fe target (1 mm thick) all from Kurt J Lesker, USA.^[17] For the MnCrFeNi films deposition, a single 3-inch (in diameter) compound target provided by Plansee was used (3 mm thick). Argon was used as the working gas with a pressure of 0.4 Pa (3 mTorr). Each target was powered by a separate HiPIMS unit (Ionautics, Sweden). All HiPIMS units were controlled by a synchronizing unit, enabling the simultaneous start of the pulses. The negative discharge pulse was 40 μ s in length at 500 Hz frequency. Before the depositions, the substrates were ultrasonically cleaned in acetone and isopropanol. The substrates were heated to 300 °C prior to and during the deposition. The films were deposited at a floating substrate potential (no voltage applied to the substrates).

Structural Characterization: The crystal structure of the films was characterized by X-ray diffraction using a Bruker D8 Discover diffractometer in a symmetric $\theta/2\theta$ configuration and Cu K α X-ray source ($\lambda = 1.5406$ Å). The morphology and chemical composition of the thin films were analyzed using SEM Sigma 300 VP Gemini (Zeiss, 5 kV acceleration voltage), and an EDS detector (Oxford Instruments X-MAX^N, 5 kV acceleration voltage) integrated in the microscope. Cross-sectional samples suitable for analysis both by SEM and (scanning) transmission electron microscopy ((S)TEM) were prepared using a dual beam SEM-focused ion beam microscope (Gemini Zeiss 1540 EsB). Pt layers were first deposited on top of the surface of the films to protect them, samples were then tilted to 36° for milling. SEM images of the cross sections were taken using the same instrument using image correction to take account of the sample tilt. Thin lamella (< 100 nm) suitable for TEM analysis were prepared using the well-established lift-out approach. TEM analysis was performed using a FEI Tecnai G2 TF 20 UT microscope operated at 200 kV acceleration voltage. High angle annular dark field (HAADF) STEM images were taken with an angular detector.

XPS was used for elemental analysis and assessment of chemical bonds. O 1s, Co 2p, Mn 2p, Cr 2p, Fe 2p, and Ni 2p core level spectra were recorded using an Axis Ultra DLD instrument from Kratos Analytical (UK) employing monochromatic Al K α radiation ($h\nu = 1486.6$ eV) and an anode power of 150 W. The base pressure during spectra acquisition was lower than 1.5×10^{-7} Pa (1.1×10^{-9} Torr). No charge compensation was used during the analysis. The analyzer pass energy was set to 20 eV resulting in the full width at half maximum of 0.55 eV for the Ag 3d_{5/2} peak of sputter-etched Ag sample used for calibration. All spectra were collected at normal emission angles. The area analyzed by XPS was 0.3×0.7 mm². As the commonly used charge referencing method relying on the C 1s peak of adventitious carbon was not reliable,^[45] all spectra were referenced to the sample Fermi edge. For sputter depth profiles, a 0.5 keV Ar⁺ ion beam was used at a 20° incident angle from the surface plane.

Electrochemical Measurements-Stationary Electrode: The electrocatalytic performance of the films was evaluated for both ORR and OER in 1 M KOH. Electrochemical measurements were carried out with a PAR-STAT 3000A-DX potentiostat. A three-electrode stationary set-up was used

where the working electrode was the thin film, an Ag/AgCl saturated with KCl ($E = 0.197$ V vs SHE) was used as reference electrode and a Pt wire as the counter electrode. The films were electrochemically activated by an anodization procedure. The first step of the anodization was applying -1 V versus Ag/AgCl for 30 min to reduce the native oxide. Then an anodic potential (0.40 V for CoCrFeNi, 0.45 V for MnCrFeNi) for 30 min to reform the oxides on the surface of the films. The anodization potential was determined from cyclic voltammograms recorded after the -1 V step, from 0 to 0.6 V with a scan rate of 5 mV s $^{-1}$. The final step of the anodization was 200 CVs to activate the surface by cycling the films between the different oxidation and reduction reactions at a high scan rate (100 mV s $^{-1}$). ORR and OER testing were carried out in O $_2$ saturated 1 M KOH with CVs measured from 0.2 to -0.8 V for ORR and 0.2 to 0.8 V for OER, both scans at the same scan rate of 5 mV s $^{-1}$.

To investigate corrosion properties of the films, they were immersed in naturally aerated 1 M KOH. The open circuit potential (OCP) was first measured for 30 min. Electrochemical Impedance Spectroscopy (EIS) was measured for all films at the different stages of anodization and catalysis testing. A perturbation of 10 mV was applied with frequencies from 100 kHz to 10 mHz. The data was analyzed and fitted to equivalent electronic circuits using the software ZSimpWin 3.60. Due to high noise in the low frequency range, only the 100 kHz– 100 mHz was considered for the fitting. Potentiodynamic polarization was carried out from -0.25 V versus OCP to 0.6 V versus Ag/AgCl with a scan rate of 1 mV s $^{-1}$. The Tafel module in the software VersaStudio was used to calculate the Tafel slopes and determine the corrosion current density i_{corr} . The extrapolation was carried out 0.1 V away from E_{corr} . All measurements were repeated for duplicate samples and carried out at room temperature.

Electrochemical Measurements—Rotating Ring Disc Electrode: To determine which reaction pathway was taken in the presence of the new catalyst, RRDE measurements were carried out. In this set-up, pure kinetic information can be accessed without any mass-transfer contribution.^[46] The films were deposited on stainless steel inserts for the RRDE set-up provided by Pine Instruments. A Bio Logic Science SP-300 bi-potentiostat was used for the measurements. A three-electrode set-up was used where the working disc electrode was the thin film, an Hg/HgO electrode ($E = 0.98$ V vs SHE) was used as reference electrode and a Pt wire as the counter electrode.

The number of electrons n were extracted from the Koutecky-Levich equation:

$$\frac{1}{I} = \frac{1}{I_K} + \frac{1}{I_L} = \frac{1}{I_K} + \frac{1}{B\omega^{1/2}} \quad (1)$$

where I is the total current density, I_K is the kinetic current, and I_L is the mass-transport (diffusion) controlled current. I_L is then dependent on the angular rotation ω . The slope B can then be extracted from the $1/I$ versus $1/\omega^{1/2}$ plots and B is defined as

$$B = 0.201nFD_0^{2/3}\nu^{-1/6}C_0 \quad (2)$$

where n is the number of transferred electrons, F is the Faraday constant, D_0 is the diffusion coefficient of oxygen, ν the kinematic viscosity of the solution, C_0 is the bulk concentration of oxygen. I_K was also extracted for Tafel slope determination.

A gold ring was used as a ring electrode for the RRDE measurements. The ring was kept at 0.3 V versus Hg/HgO to oxidize any hydrogen peroxide produced at the disc. From the ring current I_R , disc current I_D , and the collection efficiency N (0.24 for this set-up) the hydrogen peroxide yield can be calculated:

$$\psi_{\text{H}_2\text{O}_2} = \frac{2I_R}{NI_D + I_R} \quad (3)$$

The current density was normalized by the geometric area of the disc (0.247 cm 2). As the stainless-steel inserts were mirror polished prior to deposition and the films follow the substrate morphology, the surfaces

were smooth. The capacitance of the films was estimated to be ≈ 0.1 μF and thus the surface roughness of the films was negligible.

Spectroscopy—In Situ Raman: The chemical changes on the catalyst surface can be studied by Raman spectroscopy, in situ during the electrochemical measurements. Ni foam was used as flexible and porous substrate for the measurements, to enable height adjustment and flow of electrolyte in the cell. Similarly to the other methods, a Hg/HgO reference electrode and Pt wire as counter electrode were used. The 1 M KOH electrolyte was saturated with oxygen by bubbling O $_2$ gas through it for 30 min prior to the measurement. The coated Ni foam was potentiostatically polarized for 5 min before the Raman spectrum was recorded. A 532 nm laser (RGG Photonics) was used for the Raman measurements. The signal was analyzed by a Andor Kymera 328i spectrograph with a 600 mm $^{-1}$ diffraction grating. Prior to the measurement, a calibration was performed with a Si wafer.

Supporting Information

Supporting Information is available from the Wiley Online Library or from the author.

Acknowledgements

This study was performed within the Competence Centre FunMat-II and was funded by the Swedish Agency for Innovation Systems (VINNOVA, grant numbers 2022–03071, 2016–05156, 2019–04881). The authors also acknowledge the Swedish Government Strategic Research Area in Materials Science on Advanced Functional Materials at Linköping University (Faculty Grant SFO-Mat-LiU No. 2009 00971).

Conflict of Interest

The authors declare no conflict of interest.

Data Availability Statement

The data that support the findings of this study are available from the corresponding author upon reasonable request.

Keywords

anodization, bifunctional oxygen catalyst, corrosion resistance, multicomponent catalysts, PGM free catalysts

Received: October 16, 2024
Revised: December 6, 2024
Published online: January 13, 2025

- [1] T. Sun, J. Wang, C. Qiu, X. Ling, B. Tian, W. Chen, C. Su, *Adv. Sci.* **2018**, *5*, 1800036.
- [2] K. Chen, S. Kim, R. Rajendiran, K. Prabakar, G. Li, Z. Shi, C. Jeong, J. Kang, O. L. Li, *J. Colloid Interface Sci.* **2021**, *582*, 977.
- [3] G. Das, J. H. Choi, P. K. T. Nguyen, D. J. Kim, Y. S. Yoon, *Polymers* **2022**, *14*, 1197.
- [4] C. Linder, S. G. Rao, A. le Febvrier, G. Greczynski, R. Sjövall, S. Munktel, P. Eklund, E. M. Björk, *Surf. Coatings Technol.* **2020**, *404*, 126643.
- [5] Z. Wu, M. Vagin, R. Boyd, G. Greczynski, P. Ding, M. Odén, E. M. Björk, *Energy Technol.* **2022**, *10*, 2200927.

- [6] S. Arya Gopal, A. Edathiparambil Poullose, C. Sudakar, A. Muthukrishnan, *ACS Appl. Mater. Interfaces* **2021**, *13*, 44195.
- [7] S. Bag, K. Roy, C. S. Gopinath, C. R. Raj, *ACS Appl. Mater. Interfaces* **2014**, *6*, 2692.
- [8] Y. J. Sa, S. Kim, Y. Lee, J. M. Kim, S. H. Joo, *ACS Appl. Mater. Interfaces* **2023**, *15*, 31393.
- [9] Z. Wu, M. Vagin, R. Boyd, P. Ding, O. Pshyk, G. Greczynski, M. Odén, E. M. Björk, *ACS Appl. Mater. Interfaces* **2023**, *15*, 26093.
- [10] C. Li, X. Han, F. Cheng, Y. Hu, C. Chen, J. Chen, *Nat. Commun.* **2015**, *6*, 4.
- [11] Y. Konno, T. Yamamoto, T. Nagayama, *Nanoscale* **2021**, *13*, 12738.
- [12] B. Cantor, I. T. H. Chang, P. Knight, A. J. B. Vincent, *Mater. Sci. Eng. A* **2004**, *213*, 375.
- [13] L. Yu, K. Zeng, C. Li, X. Lin, H. Liu, W. Shi, H. Jun, Q. Yifei, Y. Yonggang, *Carbon Energy* **2022**, *4*, 731.
- [14] T. Löffler, H. Meyer, A. Savan, P. Wilde, A. Garzón Manjón, Y. T. Chen, E. Ventosa, C. Scheu, A. Ludwig, W. Schuhmann, *Adv. Energy Mater.* **2018**, *8*, 1802269.
- [15] S. Schumacher, S. Baha, A. Savan, C. Andronescu, A. Ludwig, *J. Mater. Chem. A* **2022**, *10*, 9981.
- [16] C. Linder, S. G. Rao, R. D. Boyd, A. Le Febvrier, P. Eklund, S. Munktel, E. M. Björk, *ACS Appl. Energy Mater.* **2022**, *5*, 10838.
- [17] C. Linder, R. Boyd, G. Greczynski, M. Vagin, D. Lundin, K. Törne, P. Eklund, E. M. Björk, *Small Sci.* **2024**, *4*, 2400296.
- [18] Critical Raw Materials Resilience: Charting a Path towards greater Security and Sustainability, <https://eur-lex.europa.eu/legal-content/EN/TXT/?uri=CELEX:52020DC0474> (accessed: September 2020).
- [19] P. Wang, S. Zhang, Z. Wang, Y. Mo, X. Luo, F. Yang, M. Lv, Z. Li, X. Liu, *J. Mater. Chem. A* **2023**, *11*, 5476.
- [20] Y. Deng, R. Zhao, *Curr. Pollut. Rep.* **2015**, *1*, 167.
- [21] G. Solomon, A. Landström, R. Mazzaro, M. Jugovac, P. Moras, E. Cattaruzza, V. Morandi, I. Concina, A. Vomiero, *Adv. Energy Mater.* **2021**, *11*, 2101324.
- [22] N. Zhang, X. Feng, D. Rao, X. Deng, L. Cai, B. Qiu, R. Long, Y. Xiong, Y. Lu, Y. Chai, *Nat. Commun.* **2020**, *11*, 4066.
- [23] S. Lee, L. Bai, X. Hu, *Angew. Chemie – Int. Ed.* **2020**, *59*, 8072.
- [24] N. Zhang, X. Feng, D. Rao, X. Deng, L. Cai, B. Qiu, R. Long, Y. Xiong, Y. Lu, Y. Chai, *Nat. Commun.* **2020**, *11*, 4066.
- [25] Y. Li, Y. Wu, M. Yuan, H. Hao, Z. Lv, L. Xu, B. Wei, *Appl. Catal. B Environ.* **2022**, *318*, 121825.
- [26] T. Huang, X. Zhang, X. Zhou, H. Zhang, X. Ma, Z. Ding, J. Yu, *Fuel* **2024**, *367*, 131559.
- [27] Z. Cui, L. Wang, H. Ni, W. Hao, C. Man, S. Chen, X. Wang, Z. Liu, X. Li, *Corros. Sci.* **2017**, *118*, 31.
- [28] D. Ma, M. Yao, K. G. Pradeep, C. C. Tasan, H. Springer, D. Raabe, *Acta Mater.* **2015**, *98*, 288.
- [29] M. K. Kini, S. Lee, A. Savan, B. Breitbach, Y. Addab, W. Lu, M. Ghidelli, A. Ludwig, N. Bozzolo, C. Scheu, D. Chatain, G. Dehm, *Surf. Coatings Technol.* **2021**, *410*, 126945.
- [30] P. B. Barna, M. Adamik, *Thin Solid Films* **1998**, *317*, 27.
- [31] F. Misják, K. H. Nagy, P. Lobotka, G. Radnóci, *J. Appl. Phys.* **2014**, *116*, 083507.
- [32] J. Y. Xie, F. L. Wang, X. J. Zhai, X. Li, Y. S. Zhang, R. Y. Fan, R. Q. Lv, Y. M. Chai, B. Dong, *Chem. Eng. J.* **2024**, *482*, 148926.
- [33] M. W. Louie, A. T. Bell, *J. Am. Chem. Soc.* **2013**, *135*, 12329.
- [34] L. Xie, P. Wang, W. Zhenga, S. Zhanb, Y. Xiab, Y. Liua, W. Yanga, Y. Li, *Proc. Natl. Acad. Sci. USA* **2023**, *120*, e2307989120.
- [35] F. Xiao, Z. Wang, J. Fan, T. Majima, H. Zhao, G. Zhao, *Angew. Chemie – Int. Ed.* **2021**, *60*, 10375.
- [36] Y. Li, C. Wang, S. Pan, X. Zhao, N. Liu, *Chemosphere* **2022**, *307*, 136074.
- [37] T. Shinagawa, A. T. Garcia-esparza, K. Takanabe, *Nat. Publ. Gr.* **2015**, *5*, 13801.
- [38] Y. Shi, L. Collins, N. Balke, P. K. Liaw, B. Yang, *Appl. Surf. Sci.* **2018**, *439*, 533.
- [39] C. Linder, S. G. Rao, R. Boyd, G. Greczynski, P. Eklund, S. Munktel, A. le Febvrier, E. M. Björk, *Thin Solid Films* **2024**, *790*, 140220.
- [40] K. D. Ralston, N. Birbilis, *Corrosion* **2010**, *66*, 075005.
- [41] J. Yang, J. Wu, C. Y. Zhang, S. D. Zhang, B. J. Yang, W. Emori, J. Q. Wang, *J. Alloys Compd.* **2020**, *819*, 152943.
- [42] H. Torbati-Sarraf, M. Shabani, P. D. Jablonski, G. J. Pataky, A. Poursaee, *Mater. Des.* **2019**, *184*, 108170.
- [43] R. F. Zhao, B. Ren, B. Cai, Z. X. Liu, G. P. Zhang, J. Jian Zhang, *Results Phys.* **2019**, *15*, 102667.
- [44] J. T. Gudmundsson, N. Brenning, D. Lundin, U. Helmersson, *J. Vac. Sci. Technol. A Vacuum, Surfaces, Film.* **2012**, *30*, 030801.
- [45] G. Greczynski, L. Hultman, *Angew. Chemie – Int. Ed.* **2020**, *59*, 5002.
- [46] J. J. Concepcion, R. A. Binstead, L. Alibabaei, T. J. Meyer, *Inorg. Chem.* **2013**, *52*, 10744.